

Article

Analysis of Melt-Pool Behaviors during Selective Laser Melting of AISI 304 Stainless-Steel Composites

Daniyal Abolhasani ^{1,2}, S. M. Hossein Seyedkashi ², Namhyun Kang ³, Yang Jin Kim ¹, Young Yun Woo ¹ and Young Hoon Moon ^{1,*}

¹ School of Mechanical Engineering, Pusan National University, Busan 46241, Korea

² Department of Mechanical Engineering, University of Birjand, Birjand 97175-376, Iran

³ School of Material Science and Engineering, Pusan National University, Busan 46241, Korea

* Correspondence: yhmoon@pusan.ac.kr; Tel.: +82-51-510-2472

Received: 29 June 2019; Accepted: 6 August 2019; Published: 8 August 2019



Abstract: The melt-pool behaviors during selective laser melting (SLM) of Al₂O₃-reinforced and a eutectic mixture of Al₂O₃-ZrO₂-reinforced AISI 304 stainless-steel composites were numerically analyzed and experimentally validated. The thermal analysis results show that the geometry of the melt pool is significantly dependent on reinforcing particles, owing to the variations in the melting point and the thermal conductivity of the powder mixture. With the use of a eutectic mixture of Al₂O₃-ZrO₂ instead of an Al₂O₃ reinforcing particle, the maximum temperature of the melt pool was increased. Meanwhile, a negligible corresponding relationship was observed between the cooling rate of both reinforcements. Therefore, it was identified that the liquid lifetime of the melt pool has the effect on the melting behavior, rather than the cooling rate, and the liquid lifetime increases with the eutectic ratio of Al₂O₃-ZrO₂ reinforcement. The temperature gradient at the top surface reduces with the use of an Al₂O₃-ZrO₂ reinforcement particle due to the wider melt pool. Inversely, the temperature gradient in the thickness direction increases with the use of an Al₂O₃-ZrO₂ reinforcement particle. The results of melt-pool behaviors will provide a deep understanding of the effect of reinforcing particles on the dimensional accuracies and properties of fabricated AISI 304 stainless-steel composites.

Keywords: selective laser melting; additive manufacturing; SLM; FEM; Al₂O₃; reinforced; Al₂O₃-ZrO₂; 304; stainless; composite

1. Introduction

Austenitic stainless steels can find more applications if their strength is improved. Hence, some studies have investigated the reinforcement of stainless steel matrices via the selective laser melting (SLM) process [1,2]. Reinforcing can be achieved through the use of Al₂O₃ to produce a metal matrix composite that exhibits high mechanical properties, in addition to high corrosion and wear resistance. However, Al₂O₃ particle has very high melting temperatures and very low thermal conductivities, which result in a very high thermal gradient during the process, causing high local stresses and crack formation [3]. The use of a eutectic mixture of Al₂O₃ and ZrO₂ powders decreases the melting temperature of Al₂O₃ from 2313 K to about 2133 K [3,4]. If an optimum volume can be identified for the samples reinforced with a eutectic mixture of Al₂O₃-ZrO₂, it can be a good alternative to strengthen the AISI 304 stainless steel.

To provide a deep understanding in relation to composites reinforced with alumina particles, this paper presents an innovative numerical study dealing with melt-pool behaviors during selective laser melting (SLM) of Al₂O₃-reinforced and a eutectic mixture of Al₂O₃-ZrO₂-reinforced AISI 304

stainless-steel composites. As is well known, the dimensional accuracies and properties of fabricated composite parts are significantly dependent on the melt-pool behaviors [2–4].

SLM is a manufacturing technique to construct three-dimensional parts in which a high-power density laser is used to melt and fuse metallic powders [4–7]. Compared with other traditional techniques, laser processing typically does not require mechanical tooling and therefore exhibits high flexibility [8–12]. In SLM, the energy density should be sufficient to ensure both the melting of the powder and the bonding of the underlying substrate. If the bonds between the scan tracks and layers are weak, defects such as cracks may be generated [13–16]. The trapped gas in the melt pool can increase the number of pores in SLM-fabricated parts. Additionally, the reduction in solubility of the element during the rapid melting and cooling process can cause detrimental defects [17]. Schleifenbaum et al. [18] found that with the increase in the laser power, the rate of material evaporation and the incidence of spattering increased. These defects should be prevented by identifying appropriate process parameters of the SLM process.

The prediction of the temperature evolution in SLM is commonly performed using the finite-element (FE) method or statistical approaches. The temperature and stress fields in samples of 90W-7Ni-3F and 316L stainless steels were predicted by Zhang et al. [19] and Hussein et al. [20]. Dai and Shaw [21] simulated the transient temperature, as well as the thermal and residual stress fields. Kundakcioglu et al. [22] performed transient thermal modeling of laser-based Additive Manufacturing (AM) for 3D freeform structures.

In the case of composites, AlMangour et al. [23] presented a simulation model for predicting the temperature evolution of the melt pool of TiC/SUS316L samples. Shi et al. [24] investigated the effects of the laser power and scan speed on the melting and solidification mechanisms during SLM of TiC/Inconel718 via a simulation approach. Li et al. [1] investigated the microstructural and mechanical properties of Al₂O₃/316L stainless-steel metal-matrix composites (MMCs) fabricated via SLM through experimental and numerical methods.

The aforementioned studies focused on a single reinforcement particle in the case of SLM of a metal matrix composite. They did not consider an SLM composite with binary-phase reinforcement, such as a eutectic mixture. The thermal cycle in the SLM process increases the complexity of the material melting and thermal behavior, if new combinations of the reinforcements are applied [25]. The melting temperature of the powder mixture is an important microstructural feature in the thermal process, as it affects the final temperature of the surface during the heating or cooling of the melt pool. No detailed analysis involving the 3D FE modeling of a selective-laser-melted part, including the metal matrix and binary-phase reinforcement and its relationship with the geometric features of the melt pool during the process, has been performed.

In this study, a eutectic mixture of Al₂O₃ and ZrO₂ powder particles was added to AISI 304 stainless steel as the metal-matrix media in a set of numerical simulation runs, incorporating experimental runs as validation tests. The use of a eutectic mixture of Al₂O₃ and ZrO₂ powders reduces the melting temperature of Al₂O₃ particles. Hence, for a better understanding of the results, both sets of parts modeled with various weight percentages of Al₂O₃ and Al₂O₃-ZrO₂ particles were considered.

For this investigation, the melt-pool dimensions and the thermal evolution of AISI 304-Al₂O₃ and AISI 304-Al₂O₃-ZrO₂ SLM composites were simulated, and the predicted thermal results were described.

2. Materials and SLM System

In this study, the eutectic mixture was prepared using powders containing 58.5 wt% Al₂O₃ and 41.5 wt% ZrO₂, corresponding to the eutectic point of the Al₂O₃-ZrO₂ binary phase diagram [4], with the reinforcement content within the AISI 304 stainless-steel powder as the metal matrix. An experiment was performed using an SLM system with a continuous-wave, ytterbium fiber laser (IPG YLR-200, IPG Photonics, Burbach, Germany), as shown in Figure 1. The maximum available power of 200 W at 6 A was used, and the laser scanning was controlled using a scanner (hurrySCAN[®]20, SCANLAB, Puchheim, Germany). Argon gas was used as a shielding gas to prevent oxidation in the

melt pool. The layering bar spread the powder, and the build cylinder moved vertically to control the powder-bed height. During the numerical and experimental runs, a 30- μm -thick layer of powder mixture was used. The laser spot diameter was fixed at 80 μm . The laser power and scanning velocity were selected after conducting a large number of preliminary experiments associated with the single-line formation tests.

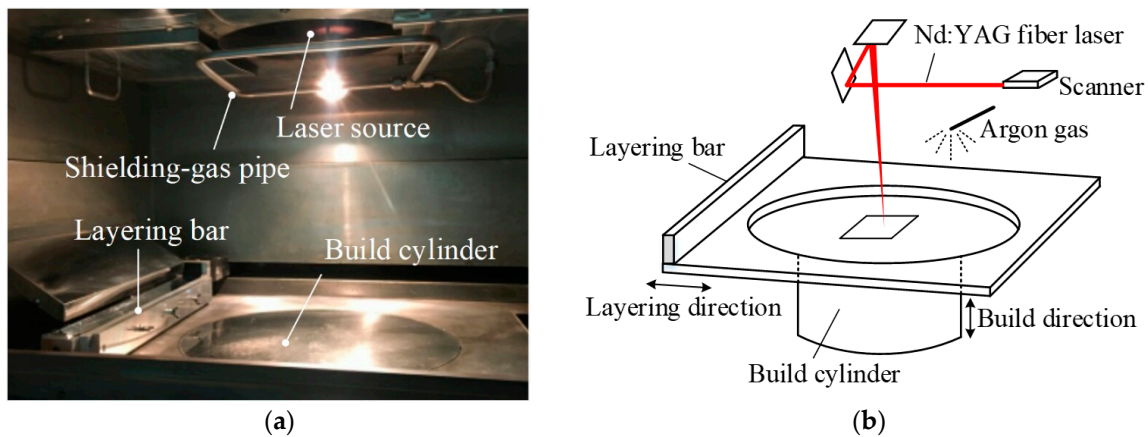


Figure 1. Selective laser melting (SLM) system: (a) Experimental setup; (b) Schematic illustration.

The laser power and scan speed were 200 W and 732 mm/s, respectively. For comprehensive comparison, various weight percentages of Al_2O_3 and the eutectic mixture of $\text{Al}_2\text{O}_3\text{-ZrO}_2$ were employed in the reinforcing experiments, as shown in Table 1.

Table 1. Numerical and experimental runs.

Ex. No.	wt% of Al_2O_3	wt% of $\text{Al}_2\text{O}_3\text{-ZrO}_2$	wt% of 304SS
1	0	0	100%
2	3%	-	97%
3	5%	-	95%
4	7%	-	93%
5	-	3%	97%
6	-	5%	95%
7	-	7%	93%

3. FE Modeling

3.1. Physical Description of Model

A 3D model was developed, and the ABAQUSTM commercial software (version 6-14, Dassault Systems, Providence, RI, USA) was utilized to simulate volumetric laser energy deposition with a Gaussian distribution. A schematic of the SLM process, which shows the interactions between the laser beam and powder bed, as well as the melting-pool dimensions and solidification, is presented in Figure 2a. A square composite powder layer with dimensions of 7 mm \times 7 mm \times 0.030 mm was placed on a stainless-steel substrate. The powder bed was meshed with eight-node linear hexahedral elements with a size of 70×10^{-6} m that were distributed uniformly throughout the powder-bed model, as shown in Figure 2b. The sweep method was used to mesh the substrate and accurately capture the flux distribution of the moving laser beam.

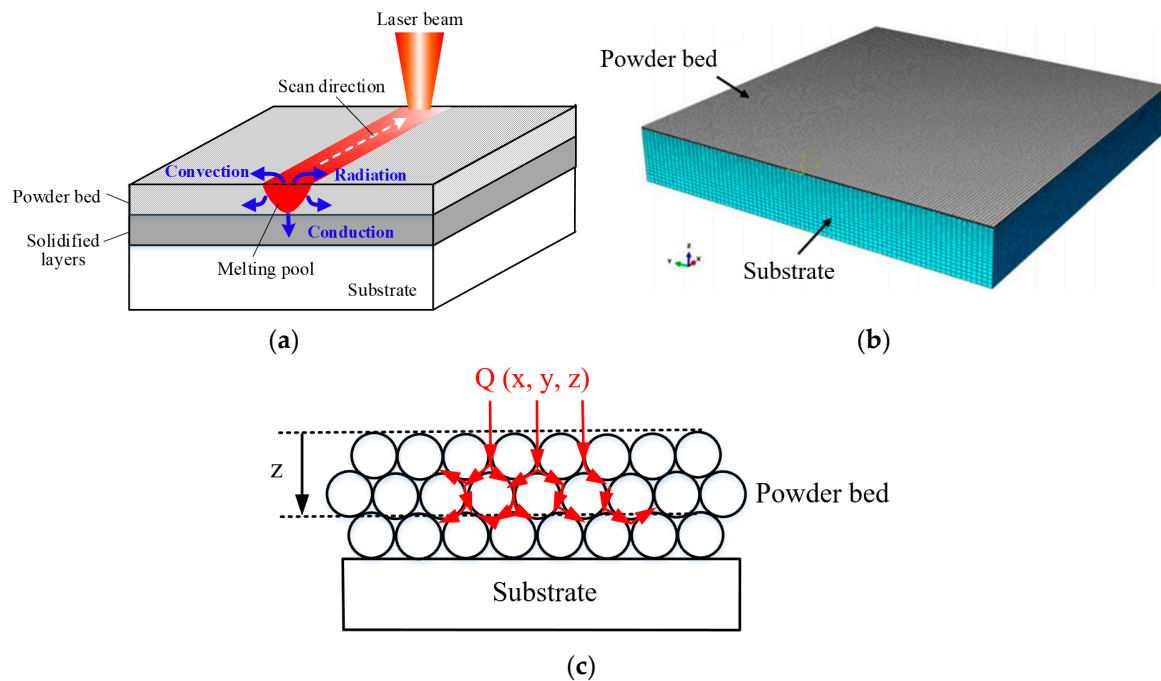


Figure 2. (a) Schematic showing the thermal behavior of the powder bed under laser irradiation. (b) 3D finite-element (FE) model. (c) Schematic showing the transfer of laser radiation into the powder bed.

3.2. Initial Governing Equation

In the powder-bed additive layer manufacturing system with a moving laser source, the heat-transport equation for 3D Cartesian coordinate systems is expressed as follows [22]:

$$\rho \cdot C_p \cdot \frac{\partial T}{\partial t} = \frac{\partial}{\partial x} \left(k \cdot \frac{\partial T}{\partial x} \right) + \frac{\partial}{\partial y} \left(k \cdot \frac{\partial T}{\partial y} \right) + \frac{\partial}{\partial z} \left(k \cdot \frac{\partial T}{\partial z} \right) + \rho \cdot C_p \cdot v \cdot \frac{\partial T}{\partial x} + Q, \quad (1)$$

where T is the temperature (K), ρ is the density (kg/m^3), C_p is the specific heat ($\text{J}/(\text{kg}\cdot\text{K})$), k is the thermal conductivity ($\text{W}/\text{m}\cdot\text{K}$), and ∇ is the differential or gradient operator. Q is the rate of internal energy conversion per unit volume (referred to as the source term, W/m^3).

The corresponding boundary condition was [20]:

$$-\frac{\partial T}{\partial z} = \frac{h}{k}(T - T_0) + \frac{\varepsilon \sigma}{k}(T^4 - T_0^4), \quad (2)$$

where T is the surface temperature of the powder bed, z is the axis perpendicular to the powder surface, $h = 200$ [26] is the forced-convection heat-transfer coefficient ($\text{W}/\text{m}^2\cdot\text{K}$) due to argon gas, $\varepsilon = 0.8$ is the emissivity of the heated surface, and $\sigma = 5.6703 \times 10^{-8} \text{ W}/\text{m}^2\cdot\text{K}^4$ is the Stefan–Boltzmann constant.

3.3. Heat-Source Model

The travel distance of the laser beam into the powder media (z), which is schematically presented in Figure 2c, can be modeled using a volumetric heat source ($Q(x, y, z)$) [27]:

$$Q(x, y, z) = (1 - R) n A \frac{P}{\pi r_0^2} \exp\left(\frac{-n(x^2 + y^2)}{r_0^2}\right) \exp\left(-\frac{1}{d} z\right), \quad (3)$$

where R is the surface reflectivity of the powder mixture, and n is a shape parameter of the heat-flux distribution, $n = 2$. A is the laser-absorption coefficient of the irradiated surface and it was modified during numerical validation. P is the laser power (W), r_0 is the laser-beam radius (m), x and y are the

Cartesian coordinates at the surface, and z is the Cartesian coordinate perpendicular to the powder bed. d is the penetration depth equal to 40 μm for the SLM process [27].

The surface reflectivity of the powder mixture (R) is expressed as follows [25,28]:

$$R = \frac{\sum_{i=1}^n \frac{R_{(i)} \beta_{(i)} w_{(i)}}{\rho_{(i)}}}{\sum_{i=1}^n \frac{\beta_{(i)} w_{(i)}}{\rho_{(i)}}}, \quad (4)$$

Here, in accordance with the three components utilized in this study (AISI 304, Al_2O_3 , and ZrO_2), n is 3; i is a subscript referring to a specific mixture component; $R_{(i)}$ is the surface reflectance of component i ; $\beta_{(i)}$ is the extinction coefficient of component i , $\rho_{(i)}$ is the density of component i , and $w_{(i)}$ is the weight percentage of component i in the mixture.

The extinction coefficient β is defined as [29]:

$$\beta = \frac{3(1-\phi)}{2\phi D}, \quad (5)$$

where ϕ is the porosity of the bed, and D is the average particle diameter of the powder. The powder density was calculated using the following equation [26]:

$$\rho_{\text{powder}} = (1 - \phi) \rho_{\text{bulk}}, \quad (6)$$

The laser-absorption coefficient of a powder bed with a Gaussian distribution (A_{powder}) was estimated using the absorption coefficient of the bulk material (A_{bulk}) [30]:

$$A_{\text{powder}} = 0.0413 + 2.89A_{\text{bulk}} - 5.36A_{\text{bulk}}^2 + 4.50A_{\text{bulk}}^3, \quad (7)$$

The values of A in Equation (3) were calculated according to the linear rule of mixtures [31]:

$$A = w_1 \cdot A_1 + w_2 \cdot A_2 + w_3 \cdot A_3, \quad (8)$$

where w_1 , w_2 , and w_3 represent the volumetric contents of the three components in the mixture, and A_1 , A_2 , and A_3 represent the absorption coefficients of the components ($\sum_{i=1}^3 w_i = 1$, $0 < A < 1$). The final values of A applied in Equation (3) were obtained through numerical validations, as discussed in Section 4.1.

The parameters presented in Table 2 were obtained from the material supplier and previous works [26,32], as well as an online source. Then, the corresponding values were calculated using Equations (4)–(8).

Table 2. Parameters used for obtaining the values of the surface reflectivity (R) and absorption coefficient (A) of the powder mixture.

Powder	$R_{(i)}$	$D_{(i)}$ (m)	$\phi_{(i)}$	ρ_{bulk} (kg/m^3)	ρ_{powder} (kg/m^3)	A_{powder}
AISI 304	0.46	20×10^{-6}	0.25	7900	5861.8	0.604
Al_2O_3	0.79	3×10^{-6}	0.65	3970	1580	0.173
ZrO_2	0.82	1×10^{-6}	0.21	6000	4740	0.266

3.4. Physical Properties of Materials

The values of k are expressed by the following equations [29,31,33], where T is the temperature and the superscripts s and m correspond to “solidus” and “melting”, respectively.

$$k = \begin{cases} \text{for AISI 304, } T < T_s : k_{\text{powder}} = k_{\text{bulk}}(1 - \phi)^n, n = 4 \\ \text{for Al}_2\text{O}_3 \text{ and ZrO}_2, T < T_s : \\ \frac{k_{\text{powder}}}{k_{\text{atm}}} = 1 - \sqrt{1 - \phi} \left(1 + \frac{\phi k_{\text{rad}}}{k_{\text{atm}}}\right) + \sqrt{1 - \phi} \left(\frac{2}{1 - \frac{k_{\text{atm}}}{k_{\text{bulk}}}} \left(\frac{1}{1 - \frac{k_{\text{atm}}}{k_{\text{bulk}}}} \ln\left(\frac{k_{\text{bulk}}}{k_{\text{atm}}}\right) - 1\right) + \frac{k_{\text{rad}}}{k_{\text{atm}}}\right), \\ \text{for all components, } T_s < T < T_m : \\ k = \left(\frac{k_0 \text{ bulk}(T_m) - k_0 \text{ powder}(T_s)}{T_m - T_s}\right) (T - T_s) + k_0 \text{ powder}(T_s) \times 10^{-3} \\ \text{for mixture, } T < T_s, T_s < T < T_m : k_{\text{mixture}} = w_1 k_1 + w_2 k_2 + w_3 k_3 \\ \text{for mixture, } T \geq T_m : \\ k_{\text{mixture}} = k_1 \left(\frac{k_2(1+2w_2) - k_1(2w_2-2)}{k_1(2+w_2) - k_2(1-w_2)}\right), w_2 < w_1, k_1 = k_1 \text{ bulk}, k_2 = k_2 \text{ bulk} \end{cases} \quad (9)$$

Here, K_{atm} is the thermal conductivity of the ambient atmosphere and is 0.018 for argon gas; ϕ is the porosity of the powder bed; k_0 is the thermal conductivity at the ambient temperature; K_{rad} is the thermal conductivity due to the radiation among the particles in the powder bed and is evaluated as in [29]:

$$K_{\text{rad}} = 4F \cdot \sigma T^3 \cdot D, \quad (10)$$

where $F = 1/3$ is the view factor; σ is the Stefan–Boltzmann constant; T is the temperature; and D is the average particle diameter of the powder.

$$C_p = \begin{cases} \text{for all components, } T_s < T < T_m : C_p = C_{p0} + \left(\frac{1}{(T_m - T_s) \sqrt{\pi}} e^{-\left(\frac{T - T_m}{T_m - T_s}\right)}\right) \times L \\ \text{for mixture, } T < T_s, T_s < T < T_m : C_{p\text{mixture}} = w_1 C_{p1} + w_2 C_{p2} + w_3 C_{p3} \\ \text{for mixture, } T \geq T_m; C_p \text{ of mixture was not available} \end{cases} \quad (11)$$

Here, C_{p0} is the specific heat capacity at the ambient temperature, L is the latent heat of melting, and C_{p1} , C_{p2} , and C_{p3} are the specific heat capacities of the three components [33].

$$\rho = \begin{cases} \text{for AISI 304, } T < T_s : \rho = \rho_1 \\ \text{for Al}_2\text{O}_3 \text{ and ZrO}_2, T < T_s : \rho = \rho_0 \\ \text{for all components, } T_s < T < T_m : \rho = \left(1 - \frac{T - T_s}{T_m - T_s}\right) \rho_0 + \left(\frac{T - T_s}{T_m - T_s}\right) \rho_0 \text{ bulk}, \\ \text{for mixture, } T < T_s, T_s < T < T_m : \rho_{\text{mixture}} = w_1 \rho_1 + w_2 \rho_2 + w_3 \rho_3 \\ \text{for mixture, } T \geq T_m : \rho_{\text{mixture}} = w_1 \rho_{\text{bulk } 1} + w_2 \rho_{\text{bulk } 2} + w_3 \rho_{\text{bulk } 3} \end{cases} \quad (12)$$

Here, ρ_1 , ρ_2 and ρ_3 are the densities of the 304 stainless-steel, Al_2O_3 and ZrO_2 powder components, respectively. ρ_0 is the density of the powder component at the ambient temperature [31,33,34]. Note that $\rho_{\text{powder}} = \rho_{\text{bulk}}$ when $\phi = 0$ at the melting point.

The phase change was included in the model by using the definition of the latent heat of melting. The T_s of the component with the lowest value (1615 K for AISI 304 stainless steel) and the T_m of the component with the highest value were used for the mixture when simulating composite parts. The solution-dependent state variables of the three fields (powder, solid, and liquid) were based on the density of the mixture (ρ) using a User Defined Field (USDFLD) subroutine.

4. Results and Discussion

To analyze melt-pool behaviors, cross-sectional views of the melt pools obtained from experimental and numerical models are compared first. Additional simulation results are then presented to exhibit the temperature effects on the liquid lifetime of the melt pools. The effect of temperature gradient on microstructural features is also discussed.

4.1. Numerical Validation and Melt-Pool Characterization

To reduce the simulation time, the single track of conditions presented in Table 1 was modeled. The numerical model was validated using the calculated dimensions of the melt pool and compared with the experimental results of the single-line formation test. Image processing was performed on the cross-sectional optical micrograph to evaluate the melt-pool morphology, as shown in Figure 3.

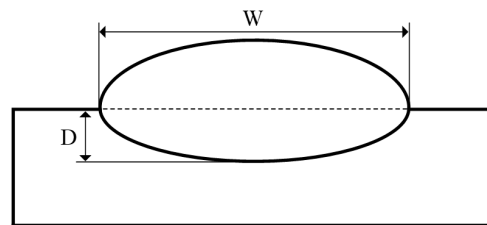


Figure 3. Schematic showing the dimensions of the melt pool. W and D represent the width (μm) and depth (μm), respectively.

The melt-pool boundary was distinguished by the melting-temperature line of the numerical-simulation thermal field. Thus, the width and depth of the numerical melt pool were compared with the average width and depth of the experimental melt pool.

Through numerical validation, the best results for the melt-pool dimensions were obtained by changing the absorption coefficient (A) of the mixture. The experimental and numerical cross-sections of three samples—pure AISI 304, 3 wt% Al_2O_3 , and 3 wt% Al_2O_3 - ZrO_2 (eutectic mixture)—are shown in Figure 4a–f. The black lines in the cross-section of the simulated conditions represent the melt-pool boundaries, which are the melting temperatures, i.e., 1670 K for pure AISI 304, 2313 K for Al_2O_3 reinforced, and 2133 K for the eutectic mixture reinforced samples [4].

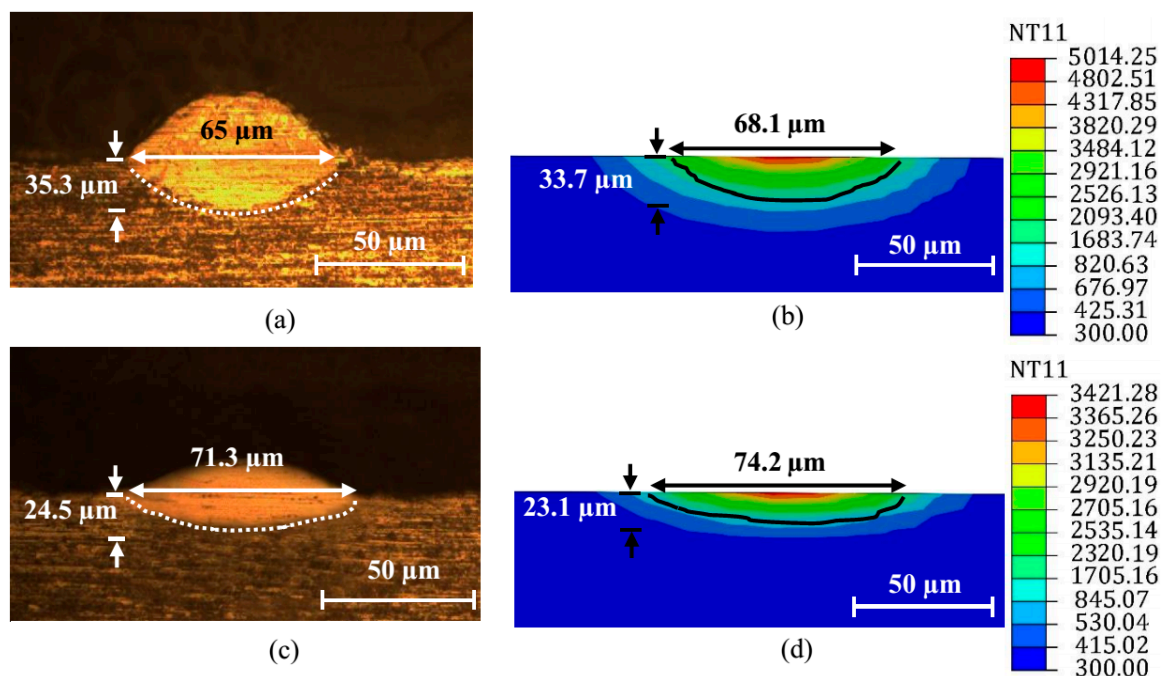


Figure 4. Cont.

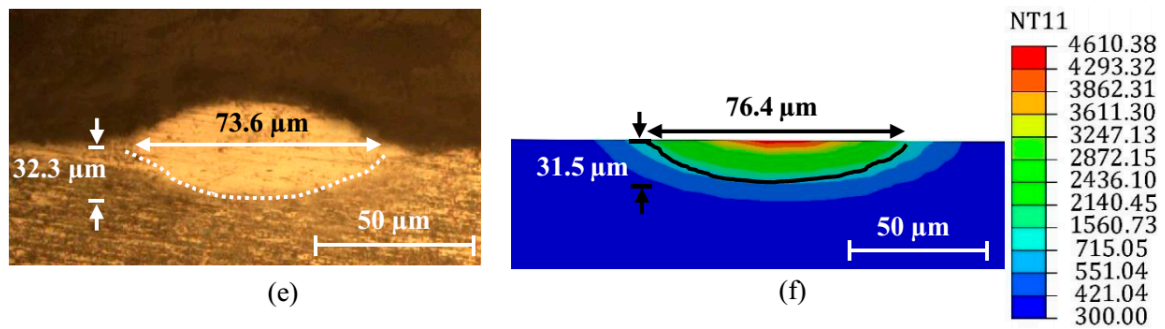


Figure 4. Cross-sectional views of the experimental and numerical models: (a,b) pure AISI 304; (c,d) 3 wt% Al₂O₃; (e,f) 3 wt% Al₂O₃-ZrO₂. (NT11: Nodal Temperature).

The experimental and numerical melt pools exhibited similar shapes. The width and depth of the melt pools under the conditions listed in Table 1 are plotted in Figure 5a,b, respectively. The two reinforced composites exhibited slight differences in width, and the width of the melt pool was smaller for the pure AISI 304 sample. As thermal conduction is the most influential factor for the melt pool [29], the results are attributed to the lower thermal conductivity in the reinforced samples compared with the pure AISI 304, as shown in Figure 5c at 800 K. The Al₂O₃-reinforced composite exhibited the smallest melt-pool depth among the samples, as it had the highest melting point, making it difficult for the molten powders to penetrate deep inside the melting pool. The larger melt-pool width and depth for the eutectic-reinforced sample compared with the Al₂O₃-reinforced sample at each weight percentage are attributed to the reduction in the melting point, along with the reduction in the thermal conductivity.

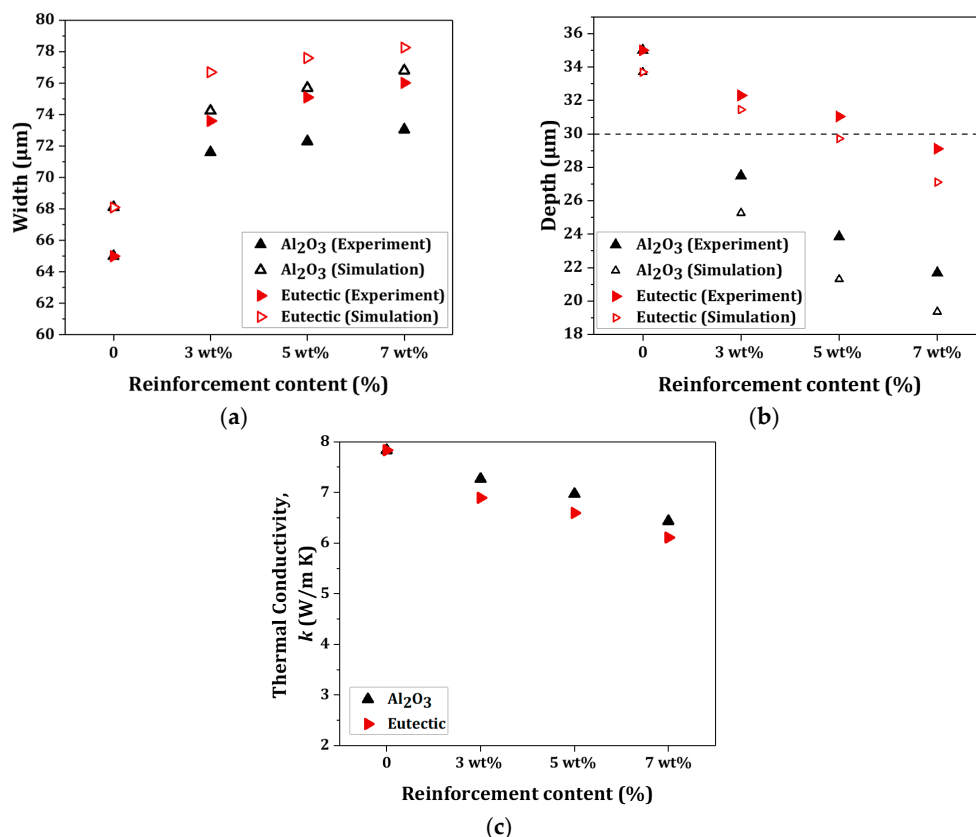


Figure 5. (a) Cross-section width and (b) depth of the experimental and numerical models. (c) Thermal conductivity (*k*) of the mixtures at 800 K.

4.2. Temperature Distribution and Liquid Lifetime

The variation of the temperature with the time needed for scanning a single path during the process, with different weight percentages of reinforcement contents, is explored. The center point of the top surface shown in Figure 6a is considered for plotting the corresponding temperature-time profiles shown in Figure 6b. Figure 6c,d also exhibit the maximum temperature of the top surface and melt-pool lifetime reaching to 300 K for each condition, respectively. As the eutectic mixture of $\text{Al}_2\text{O}_3\text{-ZrO}_2$ is replaced with the Al_2O_3 reinforcing particle, the maximum temperature is increased significantly due to the reduction in the thermal conductivity and latent heat of the mixture. Also according to Figure 6b, concerning the slope of the cooling curve as the cooling rate, this rate decreased especially in the cases with 7 wt% of reinforcement particles. The simulation results show that as the reinforcement content increases, the cooling rate decreases. The main factor affecting the maximum temperature in various weight percentages of a specific reinforcement in the simulations is identified to be the absorption coefficient. The absorption coefficient of the mixtures was calculated using Equation (8) and exhibited a decreasing trend when increasing a reinforcement content, as is shown in Figure 6e. It is important to note that the cooling rate, i.e., the slope of the cooling curve of Al_2O_3 and $\text{Al}_2\text{O}_3\text{-ZrO}_2$ systems upon each weight percentage of the reinforcing particle, showed a negligible discrepancy. From the cooling step in simulation runs, the liquid lifetime of the melt pool is distinguished. From Figure 6d, it can be seen that the liquid lifetime increases with the use of a eutectic ratio of $\text{Al}_2\text{O}_3\text{-ZrO}_2$ reinforcement. Meanwhile, it also rises as the reinforcement content increases. Because the gas atoms are released from the lattice in the heat-affected zone, yielding a longer liquid lifetime in samples with a high weight percentage of reinforcement, e.g., 7 wt%, may result in the formation of a higher amount of gas. It is reported that this phenomenon may cause the formation of porosity in SLM-produced parts [35]. This was explored by multi-line formation tests shown in Figure 7, where the presence of cracks is evident in the reinforced sample with 7 wt% $\text{Al}_2\text{O}_3\text{-ZrO}_2$, seen in Figure 7f. On the other hand, a short liquid lifetime of the melt pool combined with a lower temperature, observed in the sample with 3 wt% Al_2O_3 , is detrimental for wetting the farther gaps of powders, which generated some inter-gaps, as observed in Figure 7a. This can also be observed in Figure 5b, in which in the sample with 3 wt% Al_2O_3 is shown, and the depth of the melt pool cannot reach to the powder bed thickness indicated by the dashed line, i.e., 30 μm . This can be expanded to other reinforced samples with Al_2O_3 particles, where lower temperatures and shorter liquid lifetimes are seen compared with reinforced samples with eutectic mixtures. An appropriate weight percentage of the reinforcement particle of Al_2O_3 or the eutectic mixture of $\text{Al}_2\text{O}_3\text{-ZrO}_2$ plays an important role in the SLM process of AISI 304 stainless-steel composites. In the case of 3 wt% $\text{Al}_2\text{O}_3\text{-ZrO}_2$, the formation of an uneven surface, as observed in Figure 7d, is the reason for which it is not regarded as an optimum condition. A proper temperature to melt the particles with appropriate liquid lifetime and melt-pool depth was achieved using a 3 wt% eutectic mixture. Considering a more moderate condition for liquid lifetime, however, the sample of 5 wt% eutectic mixture shows a reasonable trend, as indicated by Figures 6b–d and 7e. From the above observation and discussion, it is evident that the melt-pool lifetime has an effect on the melting behavior, rather than the cooling rate.

4.3. Temperature Gradient

As SLM is an unsteady-state process, temperature gradients along surface direction and thickness direction are unavoidable. The heating and solidification during the process will alter the temperature gradient. This affects the microstructural features, such as grain morphology, grain size and its size distribution, as well as residual stress accumulation due to a large temperature gradient. In general, the unstable material flow, warpage and delamination between fabricated layers are detrimental results of process-induced stresses [36–38].

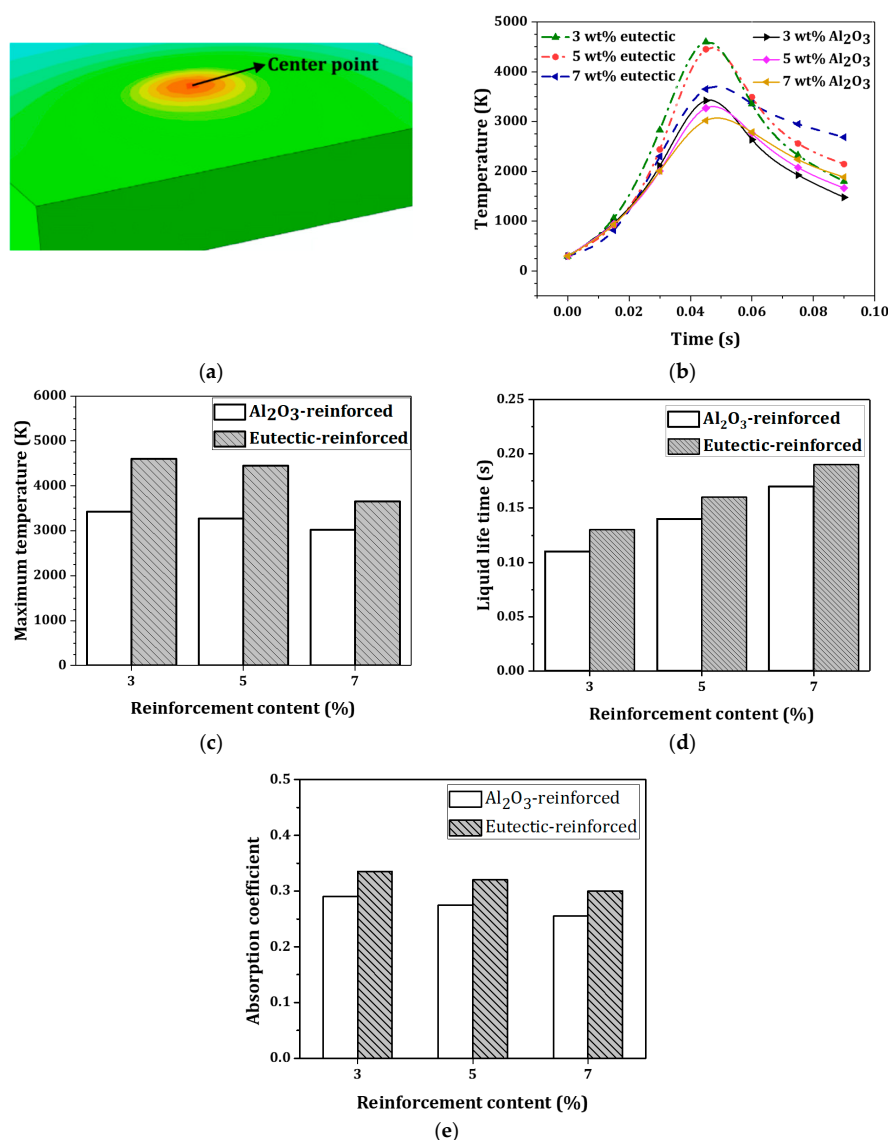


Figure 6. (a) Center point on the top surface chosen for plotting the (b) Temperature-time curves. (c) Results for the maximum temperatures of the reinforced samples. (d) Liquid lifetimes. (e) The final estimations of the absorption coefficients.

The slope of the curve of temperature distribution presents the temperature gradient of the material [20]. Figure 8a,b show the effects of reinforcement contents on the temperature distribution along the Y-direction at the top surface and Z-direction, or thickness direction, during SLM of Al₂O₃/Al₂O₃-ZrO₂, AISI 304 systems. With the use of an Al₂O₃-ZrO₂ reinforcement system, the temperature gradient at the top surface reduces. This can be recognized in Figure 8a by reducing the slope of the curve of temperature distribution compared with those of Al₂O₃ systems with similar weight percentages of reinforcement content. The generation of a wider melt pool, seen in Figure 5a, or the observation of a larger temperature distribution, seen in Figure 6b, are responsible for this observation. In Figure 8b, the temperature gradient in the thickness direction (Z-direction) of the melt pool is larger in Al₂O₃-ZrO₂-reinforced composites than those of Al₂O₃-reinforced composites. The temperature at the bottom area of the powder bed, shown on a vertical dashed line in Figure 8b, yields higher magnitudes in Al₂O₃-ZrO₂ reinforced samples, but the slope of the plot or temperature gradient in the powder bed is higher compared with Al₂O₃ samples. When a large temperature gradient in the thickness direction is accompanied by a larger depth of the melt pool, as seen in

Figure 5b, this may imply a larger dissipation of laser energy through the pre-fabricated layers or metal substrate. So, it can exert a larger liquid flow in the melt pool in $\text{Al}_2\text{O}_3\text{-ZrO}_2$ samples.

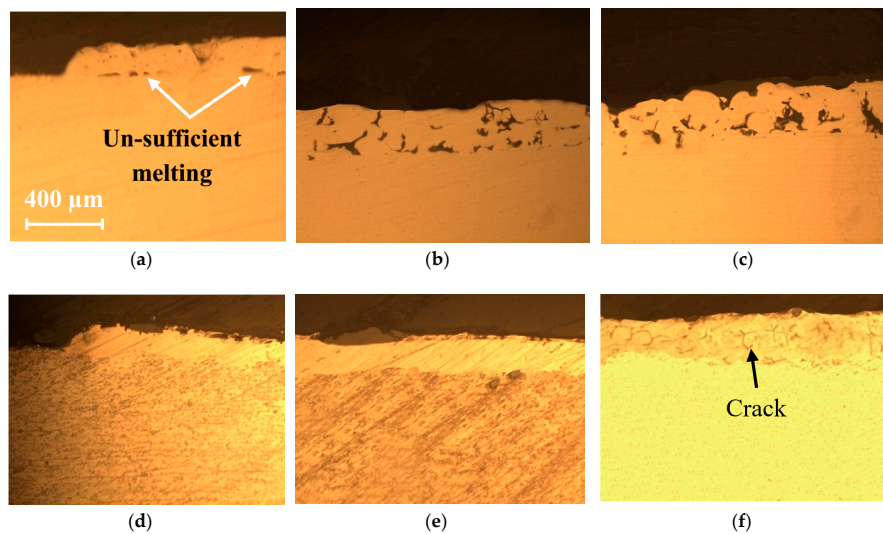


Figure 7. Optical micrographs showing the multi-line formation test results. Al_2O_3 -reinforced samples of: (a) 3 wt%, (b) 5 wt%, and (c) 7 wt%. $\text{Al}_2\text{O}_3\text{-ZrO}_2$ reinforced samples of: (d) 3 wt%, (e) 5 wt%, and (f) 7 wt%.

Liquid flow in the melt pool is an important issue in processes related to molten metals. The free surface energy, which is changed by local heating or cooling, is used to drive liquid metal. However, the term “free surface energy” is not commonly used in regard to liquids and refers to the “gradient in the surface tension” [39]. Thus, the thermal creep in different directions can be obtained by applying a temperature gradient to the surfaces, because heating a surface causes the surface tension to decrease or increase. Inhomogeneities in the gradient of the temperature of a liquid surface generate forces related to the Marangoni effect. This effect can typically be defined as a dimensionless number (M) in the characterization of flows, as indicated by Equation (13) [39].

$$M = \left| \frac{d\gamma}{dT} \right| \times \left| \frac{dT}{di} \right| \times \frac{L^2}{\mu \alpha}, \quad (13)$$

Here, $d\gamma/dT$ is the surface-tension gradient or surface-tension temperature coefficient ($\text{N m}^{-1} \text{K}^{-1}$), dT/di is the temperature gradient (K m^{-1}) along a specific direction of i , L is the characteristic length (m), μ is the dynamic viscosity ($\text{N m}^{-2} \text{s}$), and α is the thermal diffusivity ($\text{m}^2 \text{s}^{-1}$). The characteristic length (L) can be considered in processes involving melting, such as welding and AM, for generating deep penetration of surfactants, joints, or additives. For evaluating the convection of the minimum length between the highest temperature (T_{max}) and the lowest temperature ($T_{min} = 300$) along the melt-pool depth, as schematically shown in Figure 8c, the horizontal dashed line drawn at 300 K in Figure 8b can illustrate this length. Following the points of minimum temperatures in the Z-direction on the horizontal dashed line in this figure, for all the models the distance between the points of the maximum and minimum temperatures (L) decreased with the increase in the reinforcement content within the metal matrix. The decrease in the maximum temperature at the top surface observed in Figure 6c may be related to the decrease in the distance between the points of the maximum and minimum temperatures, i.e., L . However, a significant discrepancy is observed between, e.g., 3 wt% Al_2O_3 -reinforced and 3 wt% eutectic-reinforced samples and so on. From a numerical viewpoint, this may be due to the higher melting temperature and hence the smaller melt-pool depth in the Al_2O_3 -reinforced sample, as previously discussed. Because the thermocapillary (Marangoni) convection always flows from a lower-surface tension region to a higher-surface tension region [39], the larger

temperature gradient in each direction causes a larger Marangoni convection in that direction. As a result, when applying the Al_2O_3 reinforcement particle, the Marangoni flow at the top surface increases, which may benefit processes such as surface alloying/hardening. While using the Al_2O_3 - ZrO_2 reinforcement particle, the Marangoni flow at the thickness direction increases, which can benefit processes such as 3D-printing. The micro-hardness measurements of the multi-layered samples were investigated at different locations, as shown in Figure 8d, based on the American Society for Testing and Materials (ASTM) E384-16 standard. Figure 8e illustrates that with the use of reinforcement particles, an improvement in the micro-hardness of the fabricated parts is achieved. However, it can be seen that the discrepancy between the micro-hardness of Al_2O_3 -reinforced samples and the eutectic ratio of Al_2O_3 - ZrO_2 reinforced samples becomes narrower at the top layer, indicating an improvement in reinforcement particles' distribution towards the surface in Al_2O_3 -reinforced samples.

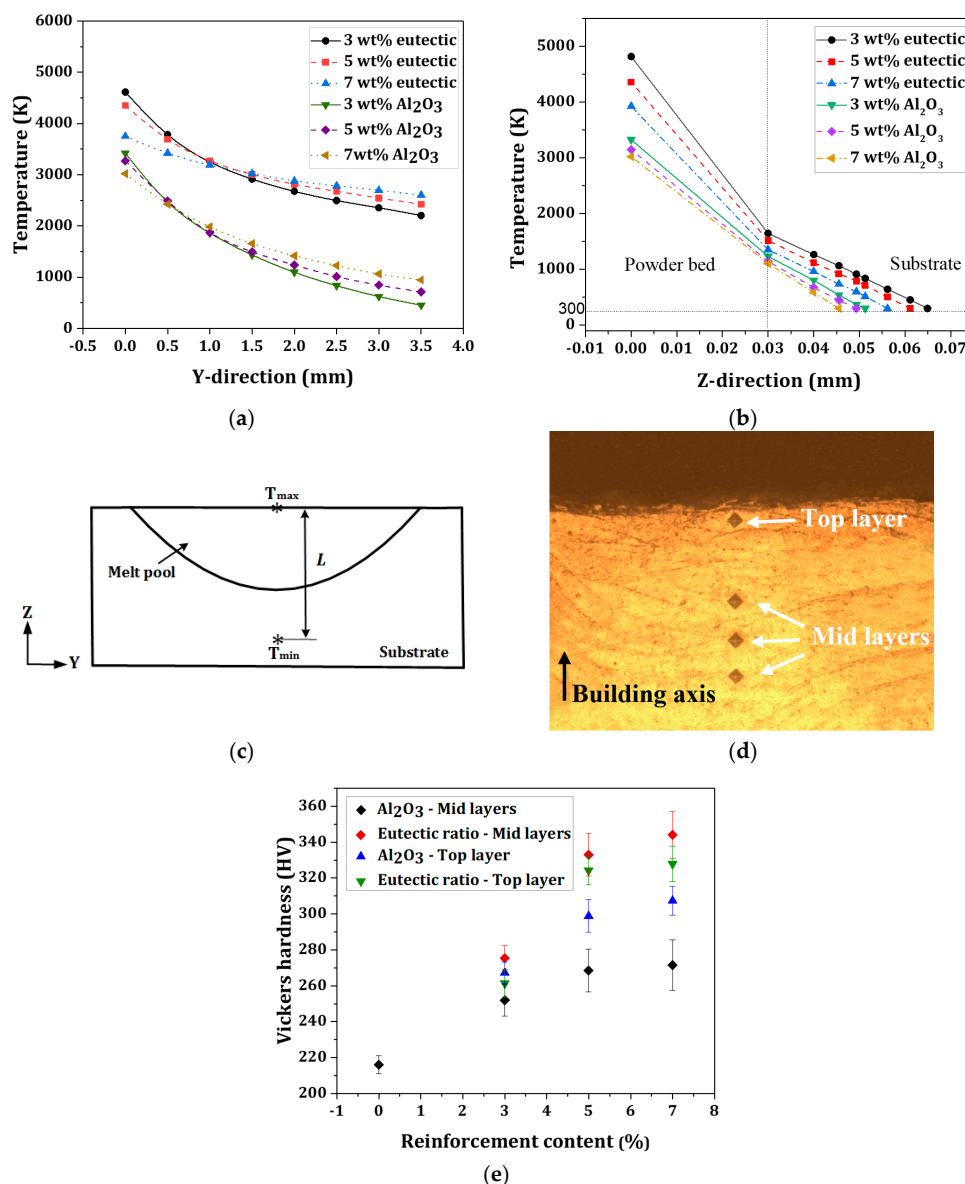


Figure 8. Temperature distribution. (a) Along the Y- direction at the top surface. (b) Along the Z-direction, i.e., thickness direction. (c) Definition of the distance between the points of the maximum and minimum temperatures (L). (d) The locations for measuring the micro-hardness. (e) Measurements of micro-hardness at different conditions and locations.

5. Conclusions

Melt-pool behaviors during selective laser melting (SLM) of Al₂O₃-reinforced and a eutectic mixture of Al₂O₃-ZrO₂-reinforced AISI 304 stainless-steel composites were analyzed both numerically and experimentally, and the following conclusions are drawn.

- (1) A 3D FE model for the SLM of Al₂O₃-reinforced and eutectic Al₂O₃-ZrO₂-reinforced AISI 304 steel composite powders was developed and successfully employed to compare the effects of the reinforcing materials on the melt-pool behaviors.
- (2) The width and depth of the melt pool were larger for the eutectic-reinforced sample, which is mainly attributed to the reduction in the melting point and thermal conductivity in this sample. With the use of the eutectic Al₂O₃-ZrO₂ instead of the Al₂O₃ reinforcing particle, the maximum temperature is increased due to the reduction in the thermal conductivity and latent heat of the mixture.
- (3) As the reinforcement content increases, the cooling rate decreases. The liquid lifetime of the melt pool has the effect on the melting behavior, rather than the cooling rate, and the liquid lifetime increases with the use of a eutectic ratio of Al₂O₃-ZrO₂ reinforcement. An average and moderate condition for the liquid lifetime was identified to be 5 wt% for the eutectic mixture.
- (4) With the use of a eutectic Al₂O₃-ZrO₂ reinforcing particle, the temperature gradient at the top surface reduces compared with the Al₂O₃-reinforced sample, due to a wider melt pool and a larger temperature distribution. This led to a narrower discrepancy between the micro-hardness of Al₂O₃-reinforced samples and the eutectic ratio of Al₂O₃-ZrO₂-reinforced samples at the top layer, indicating an improvement in reinforcement particles' distribution towards the surface in Al₂O₃-reinforced samples. The molten-pool behaviors and the thermal evolution of AISI 304 stainless-steel composites during the selective laser melting process will provide a deep understanding of the effect of reinforcing particles on the shape accuracies and properties of fabricated products.

Author Contributions: Conceptualization, Y.J.K.; Investigation, D.A. and Y.Y.W.; Methodology, S.M.H.S.; Supervision, Y.H.M.; Validation, N.K.

Funding: This work was supported by a National Research Foundation of Korea (NRF) grant (No. 2012R1A5A1048294) funded by the Korean Government (Ministry of Science, ICT and future Planning).

Conflicts of Interest: The authors declare no conflict of interest.

References

1. Li, X.; Willy, H.J.; Chang, S.; Lu, W.; Heng, T.S.; Ding, J. Selective laser melting of stainless steel and alumina composite: Experimental and simulation studies on processing parameters, microstructure and mechanical properties. *Mater. Des.* **2018**, *145*, 1–10. [[CrossRef](#)]
2. AlMangour, B.; Grzesiak, D.; Yang, J.M. Selective laser melting of TiC reinforced 316L stainless steel matrix nanocomposites: Influence of starting TiC particle size and volume content. *Mater. Des.* **2016**, *104*, 141–151. [[CrossRef](#)]
3. Yves-Christian, H.; Jan, W.; Wilhelm, M.; Konrad, W.; Reinhart, P. Net shaped high performance oxide ceramic parts by selective laser melting. *Physics Procedia* **2010**, *5*, 587–594. [[CrossRef](#)]
4. Wilkes, J.; Hagedorn, Y.C.; Meiners, W.; Wissenbach, K. Additive manufacturing of ZrO₂-Al₂O₃ ceramic components by selective laser melting. *Rapid Prototyp. J.* **2013**, *19*, 51–57. [[CrossRef](#)]
5. Jang, J.H.; Joo, B.D.; Van Tyne, C.J.; Moon, Y.H. Characterization of deposited layer fabricated by direct laser melting process. *Met. Mater. Int.* **2013**, *19*, 497–506. [[CrossRef](#)]
6. Hwang, T.W.; Woo, Y.Y.; Han, S.W.; Moon, Y.H. Fabrication of mesh patterns using a selective laser-melting process. *Appl. Sci.* **2019**, *9*, 1922. [[CrossRef](#)]
7. Joo, B.D.; Jang, J.H.; Lee, J.H.; Son, Y.M.; Moon, Y.H. Selective laser melting of Fe-Ni-Cr layer on AISI H13 tool steel. *Trans. Nonferrous Met. Soc. China* **2009**, *19*, 921–924. [[CrossRef](#)]

8. Altan, T.; Lilly, B.; Yen, Y.C.; Altan, T. Manufacturing of dies and molds. *CIRP Ann.* **2001**, *50*, 404–422. [[CrossRef](#)]
9. Kim, S.Y.; Joo, B.D.; Shin, S.; Van Tyne, C.J.; Moon, Y.H. Discrete layer hydroforming of three-layered tubes. *Int. J. Mach. Tools Manuf.* **2013**, *68*, 56–62. [[CrossRef](#)]
10. Karnati, S.; Zhang, Y.; Liou, F.F.; Newkirk, J.W. On the feasibility of tailoring copper–nickel functionally graded materials fabricated through laser metal deposition. *Metals* **2019**, *9*, 287. [[CrossRef](#)]
11. Han, S.W.; Woo, Y.Y.; Hwang, T.W.; Oh, I.Y.; Moon, Y.H. Tailor layered tube hydroforming for fabricating tubular parts with dissimilar thickness. *Int. J. Mach. Tools Manuf.* **2019**, *138*, 51–65. [[CrossRef](#)]
12. Abazari, H.D.; Seyedkashi, S.M.H.; Gollo, M.H.; Moon, Y.H. Evolution of microstructure and mechanical properties of SUS430/C11000/SUS430 composites during the laser-forming process. *Met. Mater. Int.* **2017**, *23*, 865–876. [[CrossRef](#)]
13. Zhao, J.R.; Hung, F.Y.; Lui, T.S.; Wu, Y.L. The relationship of fracture mechanism between high temperature tensile mechanical properties and particle erosion resistance of selective laser melting Ti-6Al-4V alloy. *Metals* **2019**, *9*, 501. [[CrossRef](#)]
14. Hwang, T.W.; Woo, Y.Y.; Han, S.W.; Moon, Y.H. Functionally graded properties in directed-energy-deposition titanium parts. *Opt. Laser Technol.* **2018**, *105*, 80–88. [[CrossRef](#)]
15. Jang, J.H.; Lee, J.H.; Joo, B.D.; Moon, Y.H. Flow characteristics of aluminum coated boron steel in hot press forming. *T. Nonferr. Metal. Soc.* **2009**, *19*, 913–916. [[CrossRef](#)]
16. Seo, D.M.; Hwang, T.W.; Moon, Y.H. Carbonitriding of Ti-6Al-4V alloy via laser irradiation of pure graphite powder in nitrogen environment. *Surf. Coat. Technol.* **2019**, *363*, 244–254. [[CrossRef](#)]
17. King, W.; Anderson, A.T.; Ferencz, R.M.; Hodge, N.E.; Kamath, C.; Khairallah, S.A. Overview of modelling and simulation of metal powder bed fusion process at Lawrence Livermore National Laboratory. *Mater. Sci. Technol.* **2015**, *31*, 957–968. [[CrossRef](#)]
18. Schleifenbaum, H.; Meiners, W.; Wissenbach, K.; Hinke, C. Individualized production by means of high power selective laser melting. *CIRP J. Manuf. Sci. Technol.* **2010**, *2*, 161–169. [[CrossRef](#)]
19. Zhang, D.Q.; Cai, Q.Z.; Liu, J.H.; Zhang, L.; Li, R.D. Select laser melting of W–Ni–Fe powders: Simulation and experimental study. *Int. J. Adv. Manuf. Technol.* **2010**, *51*, 649–658. [[CrossRef](#)]
20. Hussein, A.; Hao, L.; Yan, C.; Everson, R. Finite element simulation of the temperature and stress fields in single layers built without-support in selective laser melting. *Mater. Des.* **2013**, *52*, 638–647. [[CrossRef](#)]
21. Dai, K.; Shaw, L. Thermal and mechanical finite element modeling of laser forming from metal and ceramic powders. *Acta Mater.* **2004**, *52*, 69–80. [[CrossRef](#)]
22. Kundakcioglu, E.; Lazoglu, I.; Rawal, S. Transient thermal modeling of laser-based additive manufacturing for 3D freeform structures. *Int. J. Adv. Manuf. Technol.* **2016**, *85*, 493–501. [[CrossRef](#)]
23. AlMangour, B.; Grzesiak, D.; Cheng, J.; Ertas, Y. Thermal behavior of the molten pool, microstructural evolution, and tribological performance during selective laser melting of TiC/316L stainless steel nanocomposites: Experimental and simulation methods. *J. Mater. Process. Technol.* **2018**, *257*, 288–301. [[CrossRef](#)]
24. Shi, Q.; Gu, D.; Xia, M.; Cao, S.; Rong, T. Effects of laser processing parameters on thermal behavior and melting/solidification mechanism during selective laser melting of TiC/Inconel 718 composites. *Opt. Laser Technol.* **2016**, *84*, 9–22. [[CrossRef](#)]
25. Wang, L.; Jue, J.; Xia, M.; Guo, L.; Yan, B.; Gu, D. Effect of the Thermodynamic behavior of selective laser melting on the formation of in situ oxide dispersion-strengthened aluminum-based composites. *Metals* **2016**, *6*, 286. [[CrossRef](#)]
26. Fan, Z.; Lu, M.; Huang, H. Selective laser melting of alumina: A single track study. *Ceram. Int.* **2018**, *44*, 9484–9493. [[CrossRef](#)]
27. Vastola, G.; Zhang, G.; Pei, X.Q.; Zhang, Y.W. Modeling the microstructure evolution during additive manufacturing of Ti6Al4V: A comparison between electron beam melting and selective laser melting. *JOM* **2016**, *68*, 1370–1375. [[CrossRef](#)]
28. Gusarov, A.V.; Kruth, J.P. Modelling of radiation transfer in metallic powders at laser treatment. *Int. J. Heat Mass Transfer* **2005**, *48*, 3423–3434. [[CrossRef](#)]
29. Sih, S.S.; Barlow, J.W. The prediction of the emissivity and thermal conductivity of powder beds. *Part. Sci. Technol.* **2004**, *22*, 427–440. [[CrossRef](#)]

30. Boley, C.D.; Mitchell, S.C.; Rubenchik, A.M.; Wu, S.S.Q. Metal powder absorptivity: Modeling and experiment. *Appl. Optics*. **2016**, *55*, 6496. [[CrossRef](#)]
31. Angle, J.P.; Wang, Z.; Dames, C.; Mecartney, M.L. Comparison of two-phase thermal conductivity models with experiments on dilute ceramic composites. *J. Am. Ceram. Soc.* **2013**, *96*, 2935–2942. [[CrossRef](#)]
32. Spierings, A.B.; Dawson, K.; Heeling, T.; Uggowitzer, P.J.; Schäublin, R.; Palm, F.; Wegener, K. Microstructural features of Sc-and Zr-modified Al-Mg alloys processed by selective laser melting. *Mater. Des.* **2017**, *115*, 52–63. [[CrossRef](#)]
33. Loh, L.E.; Chua, C.K.; Yeong, W.Y.; Song, J.; Mapar, M.; Sing, S.L.; Liu, Z.H.; Zhang, D.Q. Numerical investigation and an effective modelling on the Selective Laser Melting (SLM) process with aluminium alloy 6061. *Int. J. Heat Mass Transfer* **2015**, *80*, 288–300. [[CrossRef](#)]
34. Mishra, A.K.; Aggarwal, A.; Kumar, A.; Sinha, N. Identification of a suitable volumetric heat source for modelling of selective laser melting of Ti6Al4V powder using numerical and experimental validation approach. *Int. J. Adv. Manuf. Technol.* **2018**, *99*, 2257–2270. [[CrossRef](#)]
35. Jeon, T.J.; Hwang, T.W.; Yun, H.J.; Van Tyne, C.J.; Moon, Y.H. Control of porosity in parts produced by a direct laser melting process. *Appl. Sci.* **2018**, *8*, 2573. [[CrossRef](#)]
36. Jeon, C.H.; Han, S.W.; Joo, B.D.; Van Tyne, C.J.; Moon, Y.H. Deformation analysis for cold rolling of Al-Cu double layered sheet by physical modeling and finite element method. *Met. Mater. Int.* **2013**, *19*, 1069–1076. [[CrossRef](#)]
37. Gordon, W.A.; Van Tyne, C.J.; Moon, Y.H. Axisymmetric extrusion through adaptable dies—Part 1: Flexible velocity fields and power terms. *Int. J. Mech. Sci.* **2007**, *49*, 86–95. [[CrossRef](#)]
38. Gordon, W.A.; Van Tyne, C.J.; Moon, Y.H. Axisymmetric extrusion through adaptable dies—Part 3: Minimum pressure streamlined die shapes. *Int. J. Mech. Sci.* **2007**, *49*, 104–115. [[CrossRef](#)]
39. AlMangour, B.; Grzesiak, D.; Borkar, T.; Yang, J.M. Densification behavior, microstructural evolution, and mechanical properties of TiC/316L stainless steel nanocomposites fabricated by selective laser melting. *Mater. Des.* **2018**, *138*, 119–128. [[CrossRef](#)]



© 2019 by the authors. Licensee MDPI, Basel, Switzerland. This article is an open access article distributed under the terms and conditions of the Creative Commons Attribution (CC BY) license (<http://creativecommons.org/licenses/by/4.0/>).